GEOLOGY

A snapshot of the long-term evolution of a distributed tectonic plate boundary

Manon Dalaison[1]*, Romain Jolivet[1,2], Laetitia Le Pourhiet[3]

Along a plate boundary, why deformation and seismic hazard distributes across multiple active faults or along a single major structure remains unknown. The transpressive Chaman plate boundary (CPB) is a wide faulted region of distributed deformation and seismicity that accommodates the differential motion between India and Eurasia at 30 mm/year. However, main identified faults, including the Chaman fault, only accommodate 12 to 18 mm/year of relative motion and large earthquakes (M_w > 7) occurred east of them. We use Interferometric Synthetic Aperture Radar to locate the missing strain and identify active structures. The current displacement is partitioned between the Chaman fault, Ghazaband fault and a recent, immature but fast fault zone to the east. Such partitioning matches known seismic ruptures and results in the ongoing widening of the plate boundary, potentially controlled by the depth of the brittle-ductile transition. The CPB illustrates the impact of geological time scale deformation on today's seismic activity.

INTRODUCTION

The relative motion of lithospheric plates at millimeters to centimeters per year results in tectonic stresses at the origin of damaging earthquakes along plate boundaries. In such regions, seismic hazard may focus on a single fault (e.g., North Anatolian fault) or be distributed across multiple structures spreading over hundreds of kilometers (e.g., the southern San Andreas fault system). There is currently little physical understanding of the mechanisms controlling strain partitioning at the scale of a plate boundary. Assessing fault-related hazard along diffuse plate boundaries requires an estimate of the distribution of available tectonic stress. A conventional approach is to map strain rates within the diffuse plate boundary (*1*). However, strain mapping is difficult in remote regions with few Global Navigation Satellite Systems (GNSS) stations like Pakistan or Afghanistan where the collision between India and Eurasia produces a wide actively deforming plate boundary (*2*).

This 200-km-wide transpressive plate boundary accommodates 28 to 36 mm/year of relative plate motion (*3*, *4*) through the interplay of a complex network of active strike-slip and compressive features along and within the orogenic belt (Fig. 1) (*5*). South of the city of Chaman, this total displacement rate is likely partitioned between several major structures striking roughly north-northeast (*6*–*8*), including the Chaman fault (CF), the Ornach Nal fault (ONF), and the Ghazaband fault (GF), among other unnamed, yet seismically active, structures. The largest recorded earthquakes occurred along the central axis (1935 M_w 7.7 Quetta earthquake) and eastern limit (e.g., 1931 M_w 7.3 Mach earthquake) of the fault system, as well as on the Hoshab fault (HF) (e.g., 2013 M_w 7.7 Balochistan earthquake), splaying west into the Makran accretionary prism (white stars in Fig. 1) (*9*–*11*). The largest recent event on the CF itself is the 1892 M_w 6.5 to 6.7 earthquake (*8*). While the seismicity distributes across the range (*10*), most studies published so far focus on elucidating the slip rate of the CF only, which only explains a fraction of the plate boundary rate (*6*, *7*, *12*, *13*), and potential additional active Quaternary structures and associated hazard are still unknown (*5*, *14*).

We elucidate the current kinematics of this plate boundary, which governs seismic hazard, and propose a mechanism to explain strain partitioning over millions of years of plate boundary evolution. We focus on the 80- to 120-km-wide plate boundary in and along the Kirthar mountain range (dashed frame on Fig. 1). We map relative ground velocities across the region using Interferometric Synthetic Aperture Radar (InSAR) and find that the largest strain gradients focus away from the main identified faults and explain the diffuse seismicity in the region. We compare the geodetically measured partitioning of strain with the long-term tectonic evolution of this margin and compare our results with the geological record and the prediction of existing long term tectonic models of transpressive plate boundaries.

Multifault model of InSAR-derived ground velocities

Ground velocity in the line of sight (LOS) direction from InSAR time series analysis is shown in Fig. 2. We build two time series spanning 2015–2020 along ascending and descending passes of the Sentinel 1A-B satellites following (*15*) and (*13*) (cf. Materials and Methods). We extract 160-km-long profiles of ground velocity perpendicular to the plate boundary every 2 km. Profiles are centered on the GF (fig. S2). After careful selection (cf. Materials and Methods), remaining surface velocity gradients, displayed in Fig. 2, are considered to be of tectonic origin.

Specifically, velocities obtained for data on the ascending track show an east-southeast gradient focusing on several elongated zones aligned with the plate boundary, while velocities from the descending track exhibit little to no strain. Given its orientation, measurements on the descending track are mostly sensitive to plate normal or vertical motion confirming the dominantly left-lateral motion across several strike-slip faults within and along the Kirthar ranges. Thrust earthquakes, reverse faults, and vertical motion in our InSAR velocities are identified along the eastern border of the ranges, outside of the area covered by our profiles (Fig. 1 and figs. S1 and S9).

[1]Laboratoire de Géologie, École Normale Supérieure, CNRS UMR 8538, PSL Université, Paris, France. [2]Institut Universitaire de France, Paris, France. [3]Sorbonne Université, CNRS-INSU, Institut des Sciences de la Terre Paris, ISTeP UMR 7193, Paris, France.
*Corresponding author. Email: dalaison@geologie.ens.fr

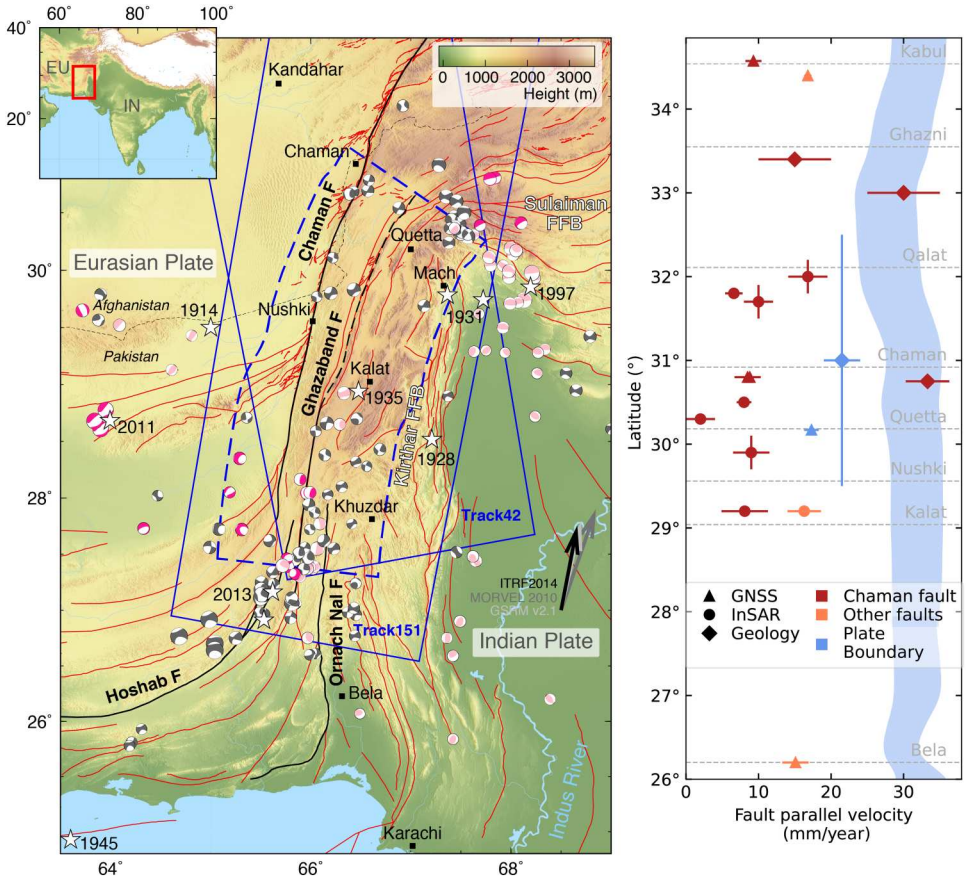

Fig. 1. Tectonic setting, current seismicity, and previous ground velocity estimates along the CF system. Left: Focal mechanisms are from the Global Centroid Moment Tensor (GCMT) and the International Seismological Center (ISC) catalogs (*49*, *50*). They are colored according to their mechanism (strike-slip in gray, normal in magenta, and reverse in pink) (fig. S1). Earthquake epicenters with M_w >7 are marked by white stars with their year of occurrence. Fault traces are from (*5*). Arrows show plate velocities of India with respect to Eurasia (*3*, *4*, *51*). Footprints of InSAR tracks are outlined in blue. Cities of reference are located by black squares. Digital Elevation Model is from (*52*). F, Fault; FFB, Fold and Fault Belt. **Right:** Summary of published strike-slip velocity estimates along the CPB. Blue symbols are estimates of the motion of India with respect to Eurasia. Red markers are slip rate estimates along the CF. Orange markers refer to other subparallel faults (ONF, GF, and Gardez fault zone). The shaded blue area is the range of relative plate motion predicted by MORVEL and ITRF14 (*3*, *4*) in the fault-parallel direction for the ONF and CF. Marker shapes indicate the type of observations. Refer to table S1 for detailed references (*6*, *7*, *12*, *53*–*57*).

We model surface strain rates induced by left-lateral slip on five faults, here assumed to be vertical, including, from west to east, the CF, the HF, the GF, and two unnamed and uncertain faults to the East. Different models with four or six faults are consistent (fig. S10). We model surface displacement in LOS as a function of the distance along the profile assuming a fault is a dislocation embedded in a semi-infinite half space (*16*). While all faults accommodate strain below a locking depth, some faults also "creep" (i.e., slip slowly aseismically) above the brittle-ductile transition (BDT), as attested on the CF (*7*, *13*) and along the HF. The interdependent parameters are explored with a Metropolis-Hastings sampling for each profile independently. Free parameters include slip rate, location and locking depth for each fault, as well as creep rate and creep depth extent for the CF and HF (see the Supplementary Materials for a priori parameterization). Because global geodetic models predict 28 to 36 mm/year relative motion across the plate boundary, we constrain the sum of left lateral slip rates on all faults to be 30 ±3 mm/year. The resulting best-fitting model leaves residuals of ±0.4 and ±0.7 mm/year for ascending and descending observations, respectively (figs. S11 and S12).

RESULTS

Figure 3 displays the inferred fault locations, slip rates, and locking depths along the plate boundary. Locking depth is shallow on the CF, especially along the segment north of Nushki, with slip rates close to 10 mm/year in agreement with previous observations and models (*6*, *7*, *12*, *13*, *17*). The GF is segmented into 50-km-long sections, which alternatingly host measurable strain or not (Fig. 3). The southernmost slipping section is located just north of a segment that ruptured in August 2020 [M_w 5.7 from Global Centroid Moment Tensor (GCMT)] and slips at a maximum rate of 14 mm/year with shallow locking depth (<1 km) at the location of the 2007 M_w 5.5 earthquake (Fig. 4) (*18*), as suggested by the sharp across-fault velocity gradients. Both other identified slipping sections of the GF host a maximum of 11 mm/year of slip below a locking depth estimated between 700 m and 9 km.

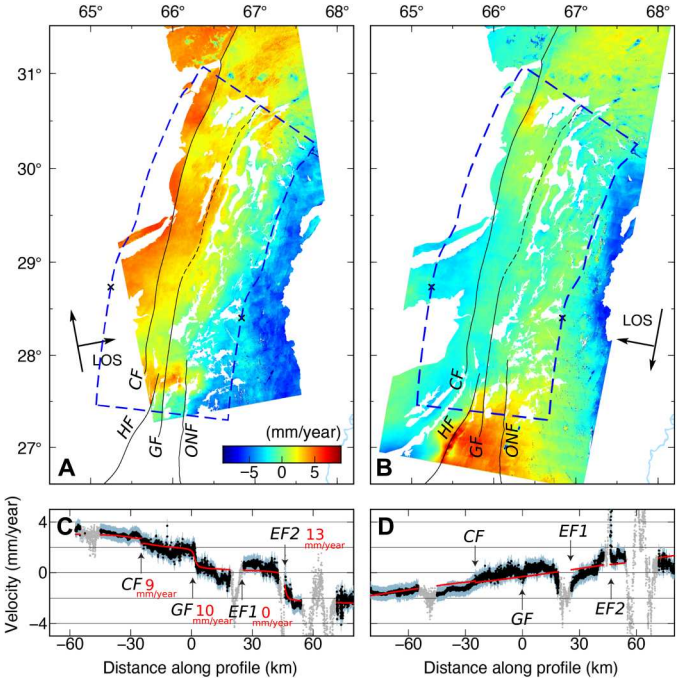

Fig. 2. Map and profile views of the measured ground velocities using InSAR. Velocities in LOS along ascending (**A**) and descending (**B**) tracks. Bottom: A sample profile in ascending (**C**) and descending (**D**) LOS, whose end points are indicated by black crosses on maps. Profiles include data kept for the model in black with light blue error bars, masked data in gray, and the predicted velocities in red from the median model with estimated fault slip values (Materials and Methods and fig. S15). Unmasked velocities and deformation maps are in figs. S3 to S6. Note that there is a large gradient in displacement rates 40 to 50 km east of the Gazhaband fault in (A) and (C) that is faint or invisible in (B) and (D), where no large tectonic structure is identified nor elevation change (figs. S8 and S9).

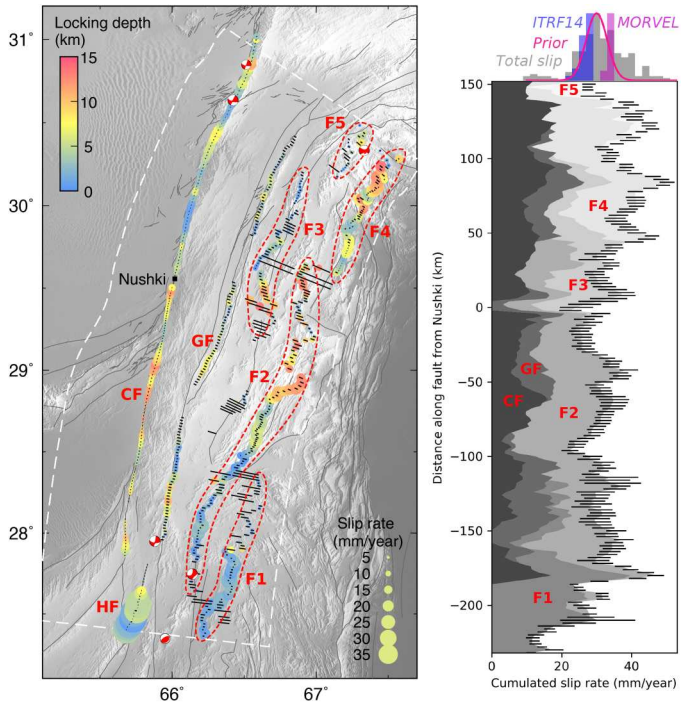

Fig. 3. Inferred fault properties: surface locations, slip rates, and locking depths. Left: Map showing the geometry of modeled faults for all profiles, overlaid on topography. The round markers locate median values, while black bars display the range between the 16th and 84th percentiles. Marker size and color depend on associated median slip rate and locking depth, respectively. The two modeled hypothetical faults east of the GF are grouped into five discrete structures (F1 to F5) based on along-strike continuity of estimated fault location (fig. S13). Red focal mechanisms are earthquakes during our observation period (fig. S4). Only points with estimated slip rate greater than 1 mm/year are represented. **Right:** Summary of measured slip rate with a cumulative *x*-scale. Each individual fault contributions are shaded in gray. Normalized distribution of slip rate values are on the top, including inferred total slip rate in gray, the prior total slip rate distribution in pink and left lateral component inferred from plate-motion models in blue and purple (*3*, *4*).

East of the GF, we group inferred locations into five continuous structures, F1 to F5 (Fig. 3 and fig. S13). Along these five faults, the median total slip rate reaches 20 (15 to 23) mm/year. Fault locations are loosely constrained although confirm what we observed in the ground velocity field. Highest slip rates, reaching 30 mm/year, are estimated in the south along F1 and F2. F2 falls in the continuation of the mapped ONF further south and the associated 2016 M_w 5.7 earthquake. It displays a shallow locking depth (2.8 km median) up to 28.8° N indicating a localized gradient, which stands out in observations (Fig. 2). North of ~29° N, locking depths exceeding 8 km for F2, F4, and parts of F3 are consistent with spread-out gradients of deformation. F3 is along the Quetta-Kalat axis with median slip rate of 7.5 (4 to 12) mm/year and a locking depth of 2.2 (0.7 to 6) km.

In the exploration for new faults, some of the estimated properties may arise from the approach taken in the model inversion and should be discarded in the interpretation. Those artifacts or unclear signals are most easily characterized by imprecise, profile-dependent fault locations. Thus, we establish that the fault at the origin of the measured strain is uncertain for the northern half of F1, as well as F2 north of Kalat and F3 south of Nushki (Fig. 3). In addition, the spotty velocity gradient at the origin of the southern half of F1 is probably of nontectonic origin (fig. S6), and we chose to remove this fault from our interpretation. Moreover, the physical meaning of F4 is uncertain due to large locking depths, interaction with the boundary of the explored space (limited by the profile length), and the potential effect of thrust motion that we do not include in our model. F5 is 40 km long and has a median slip rate of 5 (4 to 8) mm/year.

In the following, we discuss our numerical description of strain rate distribution in the context of our understanding of the plate boundary arising from seismology, geology, and geodynamics. The interpreted fault geometry is shown in Fig. 4.

DISCUSSION

Partitioning of slip and mapped structures and ruptures

Earthquakes provide the most robust evidence of current strain partitioning across the plate boundary independent of what we learn from InSAR velocities. The marked 1935 Quetta earthquake (M_w 7.7) occurred on the Quetta-Kalat fault (QKF) about 20 km east of the GF (*8*–*10*), where we identify about 8 mm/year of strain rate (F3). This active fault may extend north of Quetta, where InSAR observations are affected by anthropogenic signals and

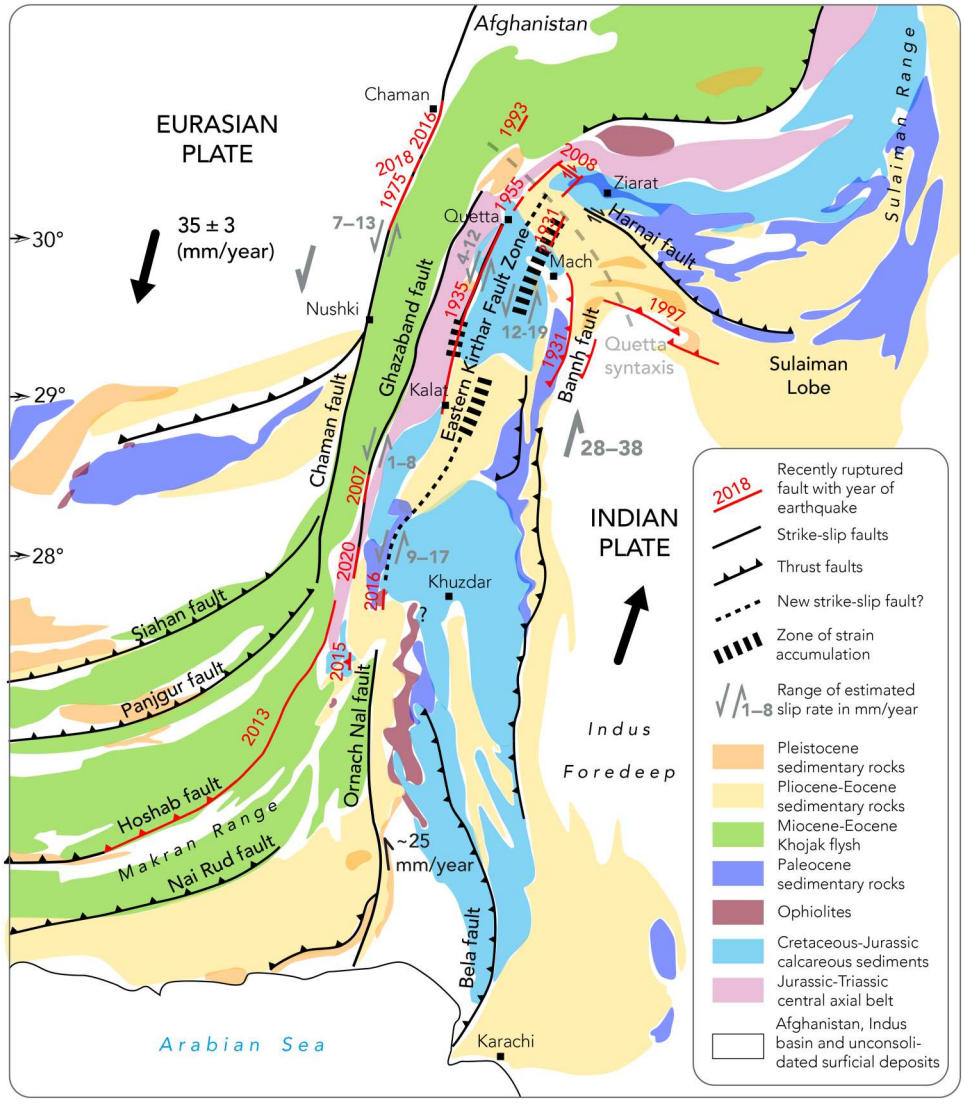

Fig. 4. Active faults and geology of the Chaman plate boundary. Geology is essentially from (*24*, *58*). Main faults only are included. Strike-slip faults with no direction of motion specified are left lateral. Mapped rupture extents are in red, and detailed references are in table S3 (*8*, *10*, *11*, *13*, *18*–*20*, *22*, *59*–*61*).

multiple ruptures of conjugate and parallel faults involved in the Ziarat earthquake sequence and its postseismic phase (*19*, *20*) suggest complex faulting and partitioning, at least in the Quetta syntaxis [the hinge between the Kirthar and Sulaiman Fold and Fault Belt (FFB)]. At those latitudes, our model identifies strain further east, with F5 15 km away and F4 just west of Mach, where the "Johan fault" is mapped (*21*).

In the 1930s, a sequence of exceptionally large earthquakes for this plate boundary outlines local partitioning of transpressive strain. The M_w 6.8 Sharigh earthquake (24 August 1931) located north of Mach with an unknown mechanism (on our F4 structure?), preceded by a few days the M_w 7.3 Mach thrust earthquake on the west dipping Bannh fault system (table S3). This thrust earthquake must have led to a reduction in normal stress along the QKF, leaving favorable stress conditions for the left-lateral Quetta earthquake in 1935 (*22*). Along the eastern border of the range, the measured ~3 mm/year gradient in both LOS directions (Fig. 2) is consistent with the GNSS-derived and modeled rate of ~5 mm/year of northwest/southeast shortening (*6*).

Identified slipping portions of the GF in the south are in agreement with contemporary seismicity (M_w 5.5 in 2007 and M_w 5.7 in 2020). Moreover, the overall secondary role of the GF in strain accommodation is consistent with published InSAR and GNSS observations (*6*, *12*). The March 2016 rupture (M_w 5.7) on the ONF and the nearby 2015 and 2020 ruptures may be related to stress transfer due to the 2013 Balochistan earthquake and its aftershocks (*11*, *23*). In turn, the 2016 earthquake may also contribute to the loading of nearby faults: the GF, and perhaps an unknown structure (F1) to the East where we measure large and sharp strain (12 to 23 mm/year), whose tectonic origin is unclear (fig. S6). Last, the northern continuation of the ONF (F2) is subparallel to the structural trends and cuts through the Kalat plateau of Eocene sedimentary rocks (yellow in Fig. 4), which is known to be faulted in its central part by the "Pandran fault" (*5*, *21*, *24*, *25*). In this region, our model

implies that the fault is locked down to about 10 km, accumulating ~2 cm/year. Past nearby earthquakes include the damaging M_w 6.2 event in March 1990 on an unknown structure with a reverse-strike-slip first motion (*10*).

Therefore, we identify deformation gradients consistent with recorded earthquake ruptures, highlighting, within this broad left-lateral shear zone, a bimodal distribution of the deformation with mature faults in the flat axial range and more segmented, immature-looking strike slip faults at the front of the range. The inferred ~30-km spacing of strike-slip faults reminds the spacing of the Californian right-lateral faults in the San Francisco Bay or Salton Sea areas, within another example of a wide and partitioned plate boundary under transpression (*1*). How do these mapped deformation gradients fit into the long-term regional tectonics and what are the rheological implication for the crust today?

Long-term evolution of the plate boundary

We focus on the straight northeast striking portion of the plate boundary, where left-lateral motion dominates, in contrast with the southern splay of thrusts in the Makran range (*25*) and the curved Sulaiman lobe to the north (*26*, *27*), two regions of shortening. The cross-sectional view in Fig. 5A synthesizes available relocated seismicity and estimated fault properties from InSAR-derived ground velocity gradients. Such partitioning of strain on numerous discontinuous faults is the signature of an unstable, evolving plate boundary which does not behave elastically at depth. In the following, we propose a dynamically consistent model of the plate boundary evolution within the long history of Eurasia-India collision (Fig. 5B).

Since about 30 Ma, as India moves North, sedimentary rocks from the Neo-Tethys ocean have piled up and are overthrusted onto the Indian plate and dragged by the indentation of India into Eurasia (*28*, *29*) to form the current CPB, a wrench-dominated FFB. Wrench-dominated FFB have mainly been modeled by the mean of brittle analog experiments (*30*, *31*) imposing a localized discontinuity at depth. These experiments display strike-slip faults, which first form as riedel shear that branch on active thrusts, until they connect to form one mature strike-slip fault, which permits to fully partition strain. Their final steady-state stage, represented as initial stage in Fig. 5B, could explain the formation of the CF, the oldest and most noticeable truncation of structural and stratigraphic trends (*32*), which would therefore act as a border fault and backstop, probably inhibiting the formation of retrovergent thrusts to the west since then. The similarities between these experiments and the distribution of the modeled strain rate along the eastern Kirthar FFB, together with the absence of

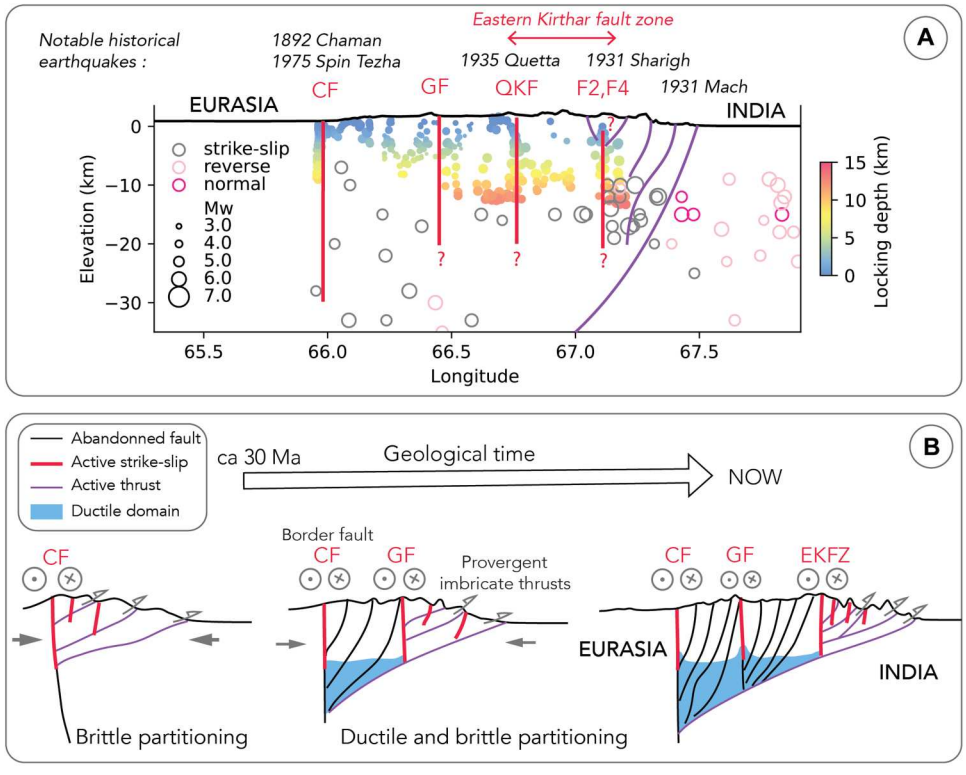

Fig. 5. Cross sections and interpreted evolution of the Chaman diffuse transpressive plate boundary. (**A**) Across-range profile (striking at 104 N) stacking the relocated seismicity (from the ISC and GCMT) and inferred fault properties below the topography at about 29° latitude. We select events and estimates between latitudes 28.3° and 30.9° and project them with a 14 N azimuth. Hence, locking depth scattering reflects along strike geometrical variations. The strong vertical exaggeration implies that low angle thrust faults (in purple) look a lot more vertical. (**B**) Schematic cross section of the proposed long-term evolution of the plate boundary kinematics leading to the current state (right). Structures at depth are inspired by numerical and analog models like (*30*, *31*, *62*) for the frontal brittle wedge structures and (*63*) for fault traces, at the rear, over the ductile decollement. Variations in BDT depth beneath strike-slip faults from (*64*, *65*) permit to localize strain during the interseismic period. With the two-dimensional simplification, we do not consider what happened in the initial frontal collision between India and Eurasia. CF, Chaman Fault; GF, Gazhaband Fault; EKFZ, Eastern Kirthar Fault Zone.

normal faults, suggest that, in this region, the imbricated frontal thrusts accommodate convergence between India and Eurasia rather than gravitational spreading (*27*). Consequently, these experiments could explain the current strain rate distribution in the eastern Kirthar FFB but not in the axial zone of the CPB.

Changes in topographic gradient observed across the CPB are similar to those produced by thermomechanical simulations of accretionary prisms, which account for a BDT with increasing burial and temperature (*33*). On the basis of these simulations, our evolution model maps the lateral extent of the flat topographic domain of the CPB domain in which BDT is reached at depth within the accretionary prism. The presence of a basal ductile layer allows strain to partition vertically, with parallel purely strike-slip faults accommodating wrenching near the surface and ductile thickening accommodating shortening at depth (*34*). Strain localization above the ductile domain might be facilitated by lateral variations of the depth of the BDT (*35*) or by the steepening of earlier thrusts facilitating potential reactivations as strike-slip fault. The QKF and northern ONF that we map indeed lie along geological boundaries (Fig. 4), and high-angle thrust faults have been mapped through seismic reflection near Quetta (*36*). Last, our proposed long-term evolution scenario (Fig. 5B) leads to today's configuration with parallel strike-slip faults within the uplifted flat axial zone and an active transpressive brittle thrust front to the east, in agreement with current displacements, seismicity, and topography. In this model, faults are simultaneously active and are currently long enough to host M_w 7.7+ earthquakes (Fig. 4). At geological time scales, according to our model, there is an eastward age progression of active structures in agreement with large-scale structural maps (*37*). We claim that current strain measurements on the comparably very short term of a few years reflect this long-term evolution with the set of immature but active fault segments to the east being the last forming strike slip structure in the system (tentatively named Eastern Kirthar Fault Zone). This system is still evolving, but it is currently impossible to assess over which time scale the surface strain we have captured will evolve in the future.

Large geodetic strain on the central and east Kirthar range fits in the long-term picture of progressive accretion, thickening, and widening of an asymmetrical transpressive margin. Thus, there is an eastward shift of the plate boundary to younger structures (controlled by the depth of the BDT), associated with the relative southward migration of the active Makran compressional wedge. Our results allow us to close the local plate boundary slip budget, which remained an enigma for several decades and the spatial distribution of seismic hazard in this region results from the long going tectonic history of the plate boundary.

MATERIALS AND METHODS

Obtaining velocities from InSAR

We base this work on InSAR velocities obtained from time series analysis. Two time series covering 2015–2020 were built along ascending (Track 42) and descending (Track 151) passes of the Sentinel 1A-B satellites (https://scihub.copernicus.eu/scihub.copernicus.eu). The data and methods are the same as in (*13*) extended in time to December 2020. Interferograms are constructed using the InSAR Scientific Computing Environment (ISCE) package and corrected from atmospheric delays with the ERA 5 global atmospheric model of the European Centre for Medium-range Weather Forecasts [PyAPS software; (*38*, *39*)]. Areas with a minimum coherence of 0.6 are unwrapped using a branch cut algorithm (*40*), and potential unwrapping errors are corrected on the basis of local misclosure [PhaCo software; (*41*)]. The best-fitting two-dimensional linear ramp northwest of the CF (fig. S3) is subtracted from each individual interferogram to remove long-wavelength biases, which may arise from orbital errors, referencing issues or ionospheric disturbances. Then, we compute the evolution of ground deformation over time with its uncertainty based on unwrapped interferograms and a parametrized model describing deformation, using a Kalman Filter–based Time Series analysis method (KFTS)(*15*). The parametrized model corresponds to a linear combination of functions of time from which the mean ground velocity in the LOS direction is obtained. Deformation related to six earthquakes (M_w ~4.5 to 5.7) in our observation frame is accounted for separately from the velocity term with the help of step functions (*13*) and is not looked at in this study (fig. S4).

Defining an appropriate model for InSAR velocities

Balochistan's dry climate and the prevailing sparsity of vegetation are particularly suitable for InSAR study yielding high coherence and velocity uncertainties typically <1 mm/year for most pixels (*13*). Velocities derived from ascending InSAR tracks are consistent with an east-southeast increasingly left-lateral velocity gradient from the edge of the Rigestan desert in south Afghanistan to the Indus plains in agreement with northward motion of India relative to Asia. In contrast, the nearly fault-parallel LOS orientation of the descending track has a poor sensitivity to left-lateral motion, except in the north, where the strike of the CF veers in a transpressional bend to a more north-easterly strike. A prominent positive velocity anomaly is imaged along and east of the HF, which we associate with postseismic deformation following the 2013 M_w 7.7 Balochistan earthquake. A negative gradient across the eastern edge of the Kirthar ranges bordering the Indus plains in both viewing directions indicates uplift rate of the order of 5 mm/year relative to the valley.

To associate LOS rates of deformation with localized strain rates on faults, we extract 160-km-long profiles normal to the mean strike of the GF at intervals of 2 km along strike. The GF is chosen as a reference as it lies in the center of our region of interest approximately parallel to the mean strike of the plate boundary (north-northeast) at this latitude (fig. S2). We ignore data near towns, cultivated areas, and mines because of the potential effect of human activities on measured ground velocities (mainly subsidence as a consequence of groundwater withdrawal). The remaining surface velocity gradients in profiles are considered to be of tectonic origin.

Fault geometries and slipping directions in the central axial belt are uncertain. While the CF trace is precisely known, other fault traces are roughly mapped from limited field work (1960s Colombo plan), aerial photography, and space-based imagery (*5*, *42*, *43*). Available focal mechanisms and historical earthquakes indicate a dominating sinistral strike-slip motion in the central axial belt (Fig. 1 and fig. S1) (*10*). Moreover, the absence of noticeable east-southeast decreasing gradient in the descending LOS within the axial belt makes InSAR-detectable thrust motion in our profiled region very unlikely (fig. S9). Thrust earthquakes, reverse faults, and vertical motion in our InSAR velocities are identified along the eastern border of the ranges, but this region is not covered by our

profiles. With this state of knowledge, the best model corresponds to slip on several strike-slip faults.

Modeling parallel strike-slip faults

Surface displacement due to a strike-slip fault is modeled by the displacement field around a screw dislocation embedded in an elastic half space (*16*). We include five faults, which are the CF, the HF, the GF, and two unnamed fault to the East (see figs. S10 and S14 for other configurations). Note that while the CF and HF locations are tightly constrained based on mapped traces, the other faults are allowed within a fairly wide distance window. We assume vertical faults for simplicity and impose fault parallel displacement consistent with left-lateral sense. The assumptions of 90 dip and zero rake are already used in (*7*) and tested in (*12*) for the case of the CF.

To limit the number of parameters to explore, we only account for shallow slip on the CF and HF. Therefore, surface displacement in LOS, f, for ascending and descending tracks (a, d superscripts) as a function of the distance, x, along the profile is modeled as

$$f(x)^{a,d} = \frac{-1}{\pi}\left[\sum_{i=1}^{5}\mathbf{u}(x)^{a,d}\mathbf{G_i}S_i\tan^{-1}\left(\frac{x-C_i}{D_i}\right) + \sum_{i=1}^{2}\mathbf{u}(x)^{a,d}\mathbf{G_i}A_i\tan^{-1}\left(\frac{E_i}{x-C_i}\right)\right] + Y^{a,d} + V^{a,d}x \quad (1)$$

with $\mathbf{u}(x)$ the varying LOS vector of sentinel 1 wide swath images, $\mathbf{G_i}$ the vector of fault orientation depending on the local fault azimuth α_i {$\mathbf{G_i}$ = [sin(α_i), cos(α_i),0]}, S_i the slip rate below a locking depth D_i on a fault located at C_i with respect to $x = 0$. Subscripts i are for each of the five faults from west to east. Creep rates and depth extents for CF and HF are A_i and E_i. Last, $Y^{a,d}$ is a constant offset of the profile and $V^{a,d}$ a slope along the whole profile length (table S2). While parameters characterizing the fault are common to the two viewing directions, parameters $Y^{a,d}$ and $V^{a,d}$ are unique to each viewing direction.

We define the posterior probability density function (PDF), p(**m**|**d**), of the model parameters, **m**, given the data, **d** as

$$\mathrm{p}(\mathbf{m}\,|\,\mathbf{d}) \propto \mathrm{p}(\mathbf{m})\mathrm{L}(\mathbf{d}\,|\,\mathbf{m}) \quad (2)$$

where p(**m**) is the a priori PDF of the model parameter defining our knowledge before collecting any data. The data likelihood, L(**d**|**m**), is a measure of the data misfit for a given model (i.e., effectively it is the probability that a given model will predict the observed data). We chose a Gaussian likelihood such as

$$\mathrm{L}(\mathbf{d}\,|\,\mathbf{m}) \propto \exp\{[f(x)^a - \mathbf{d}^a]^T(\mathbf{C}_\mathrm{d}^a)^{-1}[f(x)^a - \mathbf{d}^a] + [f(x)^d - \mathbf{d}^d]^T(\mathbf{C}_\mathrm{d}^d)^{-1}[f(x)^d - \mathbf{d}^d]\} \quad (3)$$

where $\mathbf{d}^a$ and $\mathbf{d}^d$ are the LOS velocities as a function of x along the ascending and descending tracks, respectively, and $\mathbf{C}_\mathrm{d}^a$ and $\mathbf{C}_\mathrm{d}^d$ are the corresponding covariance matrices.

Interdependent parameters in **m**, including S_i, C_i, D_i (i from 1 to 5) A_i, E_i (i in [1,2]) $Y^{a,d}$ and $V^{a,d}$, are sampled from the posterior PDF with an adaptive Metropolis-Hastings algorithm (*44*–*46*); 5×10^4 samples are drawn from the posterior PDF with an additional 1×10^4 discarded samples for the initial burn. When a fault does not cross a given profile, it is excluded from the inversion. This is true for CF in the south or HF in most profiles except in the south. For a profile crossing all five faults, there are 23 parameters to adjust.

Covariances and a priori PDF of the model parameters

We build diagonal data covariance matrices, $\mathbf{C}_\mathrm{d}^{a,d}$, implying that no spatial correlation is accounted for. The data variance is the estimated variance on LOS velocities from time series analysis (KFTS output) in addition to a prediction error with a variance set to 4 $(\mathrm{mm/year})^2$. We add a systematic prediction error to the data to account for errors resulting from the imperfect functional description in Eq. 1 (*47*, *48*).

Parameters are explored within a likely spread of natural values, accounting for our physical and tectonic understanding of the region. This limits the range of possibilities, maximizing the chance to find meaningful optima. A priori distributions in p(**m**) are truncated Gaussian functions except for slip rates S_i and the offsets Y for which a uniform distribution is preferred to minimize the role of the a priori in the final slip rate estimate (see table S2 for a complete description of a priori distributions). The CF and HF have been precisely mapped (*5*, *11*), whereas the mapped GF has several strands and the location of active faults further east is completely uncertain. Hence, the SD of the distribution of C_1 and C_2 is 250 m, while it is 1 km for C_3 and 4 km for C_4 and C_5. We also tested to constrain the QKF location, which ruptured during the 1935 earthquake (see model output in fig. S14). However, in the final model, we prefer to leave this parameter quite free to show that the data itself include a substantial strain gradient there (i.e., the data require the presence of the QKF even if we do not prescribe it).

For physical consistency, we impose that the creep extent on a given fault has to be less than the locking depth (i.e., $E_i < D_i$ for i = 1,2). Moreover, to account for what we know from global geodetic plate motion models, we add the condition that the sum of slip rates on all faults, except the HF ($S_1 + S_3 + S_4 + S_5$) should be 30 ±3 mm/year. This tectonic constraint on total slip rate limits the ambiguity between D_i and S_i. Large slip rate at depth may seem equivalent to smaller and shallower slip as seen in the joint distributions of S_i and D_i (e.g., fig. S15). Furthermore, the maximum locking depth of GF, D_3, is limited by the proximity of HF in the south so that the strong postseismic signal does not leak into the GF slip rate estimate. Maximum D_3 is then two-third of the a priori along-profile distance between both faults.

Posterior model representation

Because of the positivity constraint on slip rates (S_i) and locking depths (D_i), their posterior probability distributions are skewed. Therefore, we chose the median and interpercentile range as reference statistics. We use the range between the 16th and 84th percentiles to get closer to the usual SD representation while showing potential skewness of the distribution, particularly relevant for strictly positive variables. The estimated fault locations east of GF, namely, C_4 and C_5 as a function of profile number, are grouped with a density-based spatial clustering of applications with noise in a normalized two-dimensional space (fig. S13).

Note that we do not discuss the HF posterior model because model outputs are hardly interpretable. First, slip rates are poorly constrained as the ascending data on the western side of HF is missing. Second, the deformation pattern seems to spread across more than 100 km (Fig. 2). Potential postseimic viscous relaxation

whose spatial signature is not properly modeled with our oversimplified dislocation model might affect this part of the region.

Supplementary Materials

This PDF file includes:

Figs. S1 to S17
Tables S1 to S3
References

REFERENCES AND NOTES

1. Y. Fialko, Interseismic strain accumulation and the earthquake potential on the southern san andreas fault system. *Nature* **441**, 968–971 (2006).
2. P. Molnar, P. Tapponnier, Cenozoic tectonics of asia: Effects of a continental collision: Features of recent continental tectonics in Asia can be interpreted as results of the India-Eurasia collision. *Science* **189**, 419–426 (1975).
3. C. DeMets, R. G. Gordon, D. F. Argus, Geologically current plate motions. *Geophys. J. Int.* **181**, 1–80 (2010).
4. Z. Altamimi, L. Métivier, P. Rebischung, H. Rouby, X. Collilieux, ITRF2014 plate motion model. *Geophys. J. Int.* **209**, 1906–1912 (2017).
5. C. Ruleman, A. Crone, M. Machette, K. Haller, K. Rukstales, Map and database of probable and possible Quaternary faults in Afghanistan, in *Open-File Report 1103* (U.S. Geological Survey, 2007).
6. W. Szeliga, R. Bilham, D. M. Kakar, S. H. Lodi, Interseismic strain accumulation along the western boundary of the Indian subcontinent. *J. Geophys. Res. Solid Earth* **117**, B08404 (2012).
7. H. Fattahi, A. Amelung, InSAR observations of strain accumulation and fault creep along the Chaman fault system, Pakistan and Afghanistan. *Geophys. Res. Lett.* **43**, 8399–8406 (2016).
8. R. Bilham, N. U. Kakar, D. M. Kakar, K. Wang, R. Bürgmann, W. D. Barnhart, The 1892 Chaman, Pakistan, earthquake. *Seismol. Res. Lett.* **90**, 2293–2303 (2019).
9. C. P. Skrine, The Quetta earthquake. *Geogr. J.* **88**, 414–428 (1936).
10. N. Ambraseys, R. Bilham, Earthquakes and associated deformation in northern Baluchistan 1892-2001. *Bull. Seismol. Soc. Am.* **93**, 1573–1605 (2003).
11. R. Jolivet, Z. Duputel, B. Riel, M. Simons, L. Rivera, S. E. Minson, H. Zhang, M. A. G. Aivazis, F. Ayoub, S. Leprince, S. Samsonov, M. Motagh, E. J. Fielding, The 2013 M_w 7.7 Balochistan earthquake: Seismic potential of an accretionary wedge. *Bull. Seismol. Soc. Am.* **104**, 1020–1030 (2014).
12. W. D. Barnhart, Fault creep rates of the Chaman fault (Afghanistan and Pakistan) inferred from InSAR. *J. Geophys. Res. Solid Earth* **122**, 372–386 (2017).
13. M. Dalaison, R. Jolivet, E. van Rijsingen, S. Michel, The interplay between seismic and aseismic slip along the chaman fault illuminated by InSAR. *J. Geophys. Res. Solid Earth* **126**, e2021JB021935 (2021).
14. S. Mohadjer, T. A. Ehlers, R. Bendick, K. Stübner, T. Strube, A quaternary fault database for central asia. *Nat. Hazards Earth Syst. Sci.* **16**, 529–542 (2016).
15. M. Dalaison, R. Jolivet, A Kalman filter time series analysis method for InSAR. *J. Geophys. Res. Solid Earth* **125**, e2019JB019150 (2020).
16. J. C. Savage, R. O. Burford, Geodetic determination of relative plate motion in central California. *J. Geophys. Res.* **78**, 832–845 (1973).
17. M. Furuya, S. P. Satyabala, Slow earthquake in Afghanistan detected by InSAR. *Geophys. Res. Lett.* **35**, L06309 (2008).
18. H. Fattahi, F. Amelung, E. Chaussard, S. Wdowinski, Coseismic and postseismic deformation due to the 2007 *M*5. 5 Ghazaband fault earthquake, Balochistan, Pakistan. *Geophys. Res. Lett.* **42**, 3305–3312 (2015).
19. B. Pinel-Puysségur, R. Grandin, L. Bollinger, C. Baudry, Multifaulting in a tectonic syntaxis revealed by InSAR: The case of the ziarat earthquake sequence (Pakistan). *J. Geophys. Res. Solid Earth* **119**, 5838–5854 (2014).
20. M. Usman, M. Furuya, Complex faulting in the Quetta Syntaxis: Fault source modeling of the October 28, 2008 earthquake sequence in Baluchistan, Pakistan, based on ALOS/PALSAR InSAR data. *Earth Planets Space* **67**, 142 (2015).
21. A. H. Kazmi, R. A. Rana, *Tectonic Map of Pakistan 1: 2 000 000: Map Showing Structural Features and Tectonic Stages in Pakistan* (Geological Survey of Pakistan, 1982).
22. W. Szeliga, R. Bilham, D. Schelling, D. M. Kakar, S. Lodi, Fold and thrust partitioning in a contracting fold belt: Insights from the 1931 Mach earthquake in Baluchistan. *Tectonics* **28**, (2009).
23. K. Wang, Y. A. Fialko, *AGU Fall Meeting Abstracts* (2017), vol. 2017, pp. G43A–0910.
24. M. A. Bakr, R. O. Jackson, *Geological map of Pakistan 1:2,000,000* (Geological Survey of Pakistan and U.S. Geological Survey, 1964).
25. D. Bannert, H. A. Raza, The segmentation of the Indo-Pakistan plate. *Pakistan J. Hydrocarb. Res.* **4**, 5 (1992).
26. M. Bernard, B. Shen-Tu, W. E. Holt, D. M. Davis, Kinematics of active deformation in the Sulaiman lobe and range, Pakistan. *J. Geophys. Res. Solid Earth* **105**, 13253–13279 (2000).
27. K. Reynolds, A. Copley, E. Hussain, Evolution and dynamics of a fold-thrust belt: The Sulaiman range of Pakistan. *Geophys. J. Int.* **201**, 683–710 (2015).
28. C. M. Powell, A speculative tectonic history of pakistan and surroundings: Some constraints from the indian ocean. *Geodyn. Pakistan* **13**, 5–24 (1979).
29. P. Tapponnier, M. Mattauer, F. Proust, C. Cassaigneau, Mesozoic ophiolites, sutures, and large-scale tectonic movements in Afghanistan. *Earth Planet. Sci. Lett.* **52**, 355–371 (1981).
30. D. R. Burbidge, J. Braun, Analogue models of obliquely convergent continental plate boundaries. *J. Geophys. Res. Solid Earth* **103**, 15221–15237 (1998).
31. K. A. Leever, R. H. Gabrielsen, D. Sokoutis, E. Willingshofer, The effect of convergence angle on the kinematic evolution of strain partitioning in transpressional brittle wedges: Insight from analog modeling and high-resolution digital image analysis. *Tectonics* **30**, TC2013 (2011).
32. I. A. Jadoon, A. Khurshid, Gravity and tectonic model across the Sulaiman fold belt and the Chaman fault zone in western Pakistan and eastern Afghanistan. *Tectonophysics* **254**, 89–109 (1996).
33. S. Pajang, L. Le Pourhiet, N. Cubas, The topographic signature of temperature-controlled rheological transitions in an accretionary prism. *Solid Earth* **13**, 535–551 (2022).
34. B. Tikoff, C. Teyssier, Strain modeling of displacement-field partitioning in transpressional orogens. *J. Struct. Geol.* **16**, 1575–1588 (1994).
35. L. Le Pourhiet, B. Huet, N. Traore, Links between long-term and short-term rheology of the lithosphere: Insights from strike-slip fault modelling. *Tectonophysics* **631**, 146–159 (2014).
36. J. Huang, S. D. Khan, A. Ghulam, W. Crupa, I. A. Abir, A. Khan, D. M. Kakar, A. Kasi, N. Kakar, Study of subsidence and earthquake swarms in the western Pakistan. *Remote Sens. (Basel)* **8**, 956 (2016).
37. M. Pubellier, N. Chamot-Rooke, F. Ego, J.-C. Guezou, E. Konstantinoskaya, A. Rabaute, J. Ali, J. C. Aitchison, C. Aubourg, J. Charvet, M. Fournier, R. Hébert, L. Jolivet, C. Lepvrier, G. Mascle, I. Popolov, J.-C. Ringenbach, S. Shokalvsky, M. Sosson, J. Verges, C. Wang, Structural map of eastern eurasia, scale 1/12 500 000 (2008).
38. R. Jolivet, R. Grandin, C. Lasserre, M.-P. Doin, G. Peltzer, Systematic InSAR tropospheric phase delay corrections from global meteorological reanalysis data. *Geophys. Res. Lett.* **38**, L17311 (2011).
39. R. Jolivet, P. S. Agram, N. Y. Lin, M. Simons, M.-P. Doin, G. Peltzer, Z. Li, Improving InSAR geodesy using global atmospheric models. *J. Geophys. Res. Solid Earth* **119**, 2324–2341 (2014).
40. R. M. Goldstein, C. L. Werner, Radar interferogram filtering for geophysical applications. *Geophys. Res. Lett.* **25**, 4035–4038 (1998).
41. A. Benoit, B. Pinel-Puysségur, R. Jolivet, C. Lasserre, CorPhU: An algorithm based on phase closure for the correction of unwrapping errors in SAR interferometry. *Geophys. J. Int.* **221**, 1959–1970 (2020).
42. A. G. Jones, B. E. Manistere, R. L. Oliver, G. S. Willson, H. S. Scott, Reconnaissance geology of part of west Pakistan, *Tech. rep*., A Colombo Plan Co-Operative Project: Hunting Survey Corporation (Government of Canada, 1961).
43. J. B. Auden, Afghanistan-west pakistan. *Geol. Soc. Lond. Spec. Publ.* **4**, 235–253 (1974).
44. N. Metropolis, S. Ulam, The Monte Carlo method. *J. Am. Stat. Assoc.* **44**, 335–341 (1949).
45. N. Metropolis, A. W. Rosenbluth, M. N. Rosenbluth, A. H. Teller, E. Teller, Equation of state calculations by fast computing machines. *J. Chem. Phys.* **21**, 1087–1092 (1953).
46. J. Salvatier, T. V. Wiecki, C. Fonnesbeck, Probabilistic programming in python using PyMC3. *PeerJ Comput. Sci.* **2**, e55 (2016).
47. A. Tarantola, *Inverse Problem Theory and Methods for Model Parameter Estimation*(SIAM, 2005), vol. 89 .
48. Z. Duputel, P. S. Agram, M. Simons, S. E. Minson, J. L. Beck, Accounting for prediction uncertainty when inferring subsurface fault slip. *Geophys. J. Int.* **197**, 464–482 (2014).
49. International seismological centre on-line bulletin; www.isc.ac.uk/iscbulletin/search/catalogue/ [accessed 14 October 2022].
50. G. Ekström, M. Nettles, A. Dziewoński, The global CMT project 2004–2010: Centroid-moment tensors for 13,017 earthquakes. *Phys. Earth Planet. In.* **200**, 1–9 (2012).
51. C. Kreemer, G. Blewitt, E. C. Klein, A geodetic plate motion and global strain rate model. *Geochem. Geophys. Geosyst.* **15**, 3849–3889 (2014).
52. T. G. Farr, P. A. Rosen, E. Caro, R. Crippen, R. Duren, S. Hensley, M. Kobrick, M. Paller, E. Rodriguez, L. Roth, D. Seal, S. Shaffer, J. Shimada, J. Umland, M. Werner, M. Oskin, D. Burbank, D. Alsdorf, The shuttle radar topography mission. *Rev. Geophys.* **45**, RG2004 (2007).

53. N. Beun, P. Bordet, J.-P. Carbonnel, Premières données quantitatives relatives au coulissage du décrochement de Chaman (Afghanistan du sud-est). *Comptes rendus hebdomadaires des seéances de l'Acadeémie des Sciences* **288**, 931–934 (1979).
54. R. D. Lawrence, S. H. Khan, T. Nakata, Chaman fault, Pakistan-Afghanistan. *Ann. Tectonicae* **6**, 196–223 (1992).
55. S. Mohadjer, R. Bendick, A. Ischuk, S. Kuzikov, A. Kostuk, U. Saydullaev, S. Lodi, D. M. Kakar, A. Wasy, M. A. Khan, P. Molnar, R. Bilham, A. V. Zubovich, Partitioning of India-Eurasia convergence in the Pamir-Hindu Kush from GPS measurements. *Geophys. Res. Lett.* **37**, L04305 (2010).
56. S. Ul-Hadi, S. D. Khan, L. A. Owen, A. S. Khan, K. A. Hedrick, M. W. Caffee, Slip-rates along the Chaman fault: Implication for transient strain accumulation and strain partitioning along the western Indian plate margin. *Tectonophysics* **608**, 389–400 (2013).
57. W. E. Crupa, S. D. Khan, J. Huang, A. S. Khan, A. Kasi, Active tectonic deformation of the western Indian plate boundary: A case study from the Chaman fault system. *J. Asian Earth Sci.* **147**, 452–468 (2017).
58. F. Maldonado, J. M. Mengal, S. H. Khan, J.-C. Thomas, *Digital Geologic Map and Landsat Image Map of Parts of Loralai, Sibi, Quetta, and Khuzar Divisions, Balochistan Province, West-Central Pakistan* (U.S. Department of the Interior, U.S. Geological Survey, 2011).
59. A. H. Kazmi, Active fault system in pakistan, in *Geodynamics of Pakistan* (Geological Survey of Pakistan Quetta, 1979), pp. 285–294.
60. W. Szeliga, S. Hough, S. Martin, R. Bilham, Intensity, magnitude, location, and attenuation in India for felt earthquakes since 1762. *Bull. Seismol. Soc. Am.* **100**, 570–584 (2010).
61. E. Nissen, J. R. Elliott, R. A. Sloan, T. J. Craig, G. J. Funning, A. Hutko, B. E. Parsons, T. J. Wright, Limitations of rupture forecasting exposed by instantaneously triggered earthquake doublet. *Nat. Geosci.* **9**, 330–336 (2016).
62. K. McClay, P. Whitehouse, T. Dooley, M. Richards, 3D evolution of fold and thrust belts formed by oblique convergence. *Mar. Pet. Geol.* **21**, 857–877 (2004).
63. C. Teyssier, B. Tikoff, Strike-slip partitioned transpression of the San Andreas fault system: A lithospheric-scale approach. *Geol. Soc. Lond. Spec. Publ.* **135**, 143–158 (1998).
64. T. Yamasaki, T. J. Wright, G. A. Houseman, Weak ductile shear zone beneath a major strike-slip fault: Inferences from earthquake cycle model constrained by geodetic observations of the western North Anatolian fault zone. *J. Geophys. Res. Solid Earth* **119**, 3678–3699 (2014).
65. N. Traore, L. Le Pourhiet, J. Frelat, F. Rolandone, B. Meyer, Does interseismic strain localization near strike-slip faults result from boundary conditions or rheological structure? *Geophys. J. Int.* **197**, 50–62 (2014).
66. W. Szeliga, Historical and modern seismotectonics of the Indian plate with an emphasis on its western boundary with the Eurasian plate, Ph.D. thesis, Citeseer (2010).
67. J. A. Álvarez-Gómez, Fmc–earthquake focal mechanisms data management, cluster and classification. *SoftwareX* **9**, 299–307 (2019).
68. P. Segall, Chap. 2 Dislocation models of strike-slip faults, in *Earthquake and Volcano Deformation* (Princeton Univ. Press, 2010).

Acknowledgments: This work benefited from rich and constructive discussions with N. Chamot-Rooke and A. Janin. We would like to thank R. Bürgmann and two anonymous reviewers, who greatly helped improve this manuscript with their insightful comments. **Funding:** This work received funding from the European Research Council (ERC) under the European Union's Horizon 2020 research and innovation program (Geo-4D project, grant agreement 758210). R.J. acknowledges funding from the Institut Universitaire de France.
Author contributions: All authors contributed to the data analysis and manuscript preparation. M.D. processed the data, conceptualized the study, and wrote the initial draft. R.J. and L.L.P provided critical feedback, validated the study, and edited the manuscript. R.J. acquired financial support. **Competing interests:** The authors declare that they have no competing interests. **Data and materials availability:** All data needed to evaluate the conclusions in the paper are present in the paper and/or the Supplementary Materials. Processed data represented in figures, including InSAR velocities and model outputs, are archived on Zenodo (https://doi.org/10.5281/zenodo.7662748).

Submitted 29 June 2022
Accepted 16 March 2023
Published 19 April 2023
10.1126/sciadv.add7235